photonics

MDPI

Article

High-Precision Endoscopic Shape Sensing Using Two Calibrated Outer Cores of MC-FBG Array

Bo Xia [1,†], Chujie Tu [2,†], Weiliang Zhao [1,3], Xiangpeng Xiao [1], Jialei Zuo [1], Yan He [1,4,*] and Zhijun Yan [1,3]

[1] School of Optical and Electronic Information, Huazhong University of Science and Technology, Wuhan 430074, China; yanzhijun@hust.edu.cn (Z.Y.)
[2] College of Basic Medical Sciences, Tongji Medical College, Huazhong University of Science and Technology, Wuhan 430030, China
[3] Optics Valley Laboratory, Wuhan 430074, China
[4] Department of Comprehensive Ultrasound Image, Zhongnan Hospital Affliated to Wuhan University, Wuhan 430071, China
* Correspondence: zn003020@whu.edu.cn
† These authors contributed equally to this work and share first authorship.

Abstract

We present a high-precision endoscopic shape-sensing method using only two calibrated outer cores of a multicore fiber Bragg grating (MC-FBG) array. By leveraging the geometric relationship among two non-collinear outer cores and the central core, the method estimates curvature and bending angle without relying on multiple outer-core channels, thereby reducing complexity and error propagation. On canonical shapes, the proposed method achieves maximum relative reconstruction errors of 1.62% for a 2D circular arc and 2.81% for a 3D helix, with the corresponding RMSE values reported for completeness. In addition, representative endoscope-relevant configurations including the α-loop, reversed α-loop, and N-loop are accurately reconstructed, and temperature tests over 25–81 °C further verify stable reconstruction performance under thermal disturbances. This work provides a resource-efficient and high-fidelity solution for endoscopic shape sensing with strong potential for integration into next-generation image-guided and robot-assisted surgical systems.

Keywords: fiber Bragg grating; 3D shape sensing; wavelength-division multiplexing; multi-core fiber

1. Introduction

Three-dimensional (3D) shape sensing is reshaping endoscopy for minimally invasive surgery. Conventional systems provide only two-dimensional (2D) views with limited depth cues, complicating navigation through tortuous anatomy [1–3]. By reconstructing the 3D configuration of endoscope in real time—position, curvature and tip pose—shape sensing restores spatial awareness, enables precise lesion localization and instrument guidance, and reduces iatrogenic injury. Continuous shape monitoring also flags excessive bending or looping that can increase patient discomfort and procedural risk, while data-driven feedback supports operator training and helps standardize performance [4–6]. When integrated with image guidance or robotic platforms, it enables closed-loop control and more reliable, efficient workflows [7–10]. Together, these capabilities mark a decisive step toward intelligent, data-driven endoscopy.

Established methods (e.g., electromagnetic tracking [11–13], image-based techniques [14–16]) provide partial solutions but have limitations including interference, tissue

Check for updates

Received: 9 December 2025
Revised: 5 January 2026
Accepted: 19 January 2026
Published: 20 January 2026

Copyright: © 2026 by the authors. Licensee MDPI, Basel, Switzerland. This article is an open access article distributed under the terms and conditions of the Creative Commons Attribution (CC BY) license.

deformation, motion blur, and complex calibration; by contrast, fiber-optic shape sensing (FOSS) enables continuous, high-precision, real-time endoscope shape reconstruction, making it a promising alternative [17,18]. The principle of the FOSS is to convert multi-channel strain measurements from fully/quasi distributed sensors into 3D curvature, and then recover the 3D spatial coordinates of the sensing fiber via a shape-reconstruction algorithm. For short-range applications (from tens of centimeters to tens of meters), the distributed strain sensing approaches are optical frequency-domain reflectometry (OFDR) [19–22] and wavelength-division multiplexing (WDM) [4,7,17]. OFDR systems achieve distributed, high-spatial-resolution strain measurements along the fiber—up to tens of micrometers—by beat-frequency detection; however, the need for an expensive tunable laser source (TLS) limits their practical deployment. In contrast, WDM systems estimate strain from shifts in the Bragg wavelength of a fiber Bragg grating (FBG) array. By precisely controlling the FBG spacing during fabrication, spatial resolutions of a few millimeters to a few centimeters can be obtained. As a more mature and cost-effective demodulation scheme, WDM is well suited for use as an auxiliary modality for endoscopic navigation [4]. For fiber-optic shape sensors, configurations based on fiber bundles [23,24] or on bonding multiple fibers to an elastic substrate (e.g., nickel–titanium, NiTi, wire) [25,26] offer high sensitivity; however, they involve complex packaging and exhibit pronounced geometric mismatch, which can compromise reconstruction accuracy. In contrast, MCF has compact core layout and well-defined geometry, enables accurate 3D shape sensing. Current MCF-based shape-sensing fibers typically employ three or more outer cores surrounding a central core [21,27], and estimate curvature magnitude and bending direction using the apparent-curvature method (ACM). Nevertheless, each outer-core channel is subject to strain-measurement error; therefore, using an excessive number of outer cores can degrade sensing accuracy and increase computational complexity, which is undesirable for real-time, high-precision endoscopic shape sensing. Meng et al. [22] proposed a shape-reconstruction strategy based on projecting the curvature vector onto the directions of two outer cores, which substantially reduces the required number of cores and simplifies the system. However, the method does not calibrate the geometric parameters of the outer cores, including the core spacing, defined as the distance from an outer core to the central core, and the core angles, defined as the included angle formed by the lines connecting the two selected outer cores to the central core. Consequently, its shape-reconstruction error is comparable to that of multi-outer-core configurations that use the ACM.

To overcome limitations of conventional MCF-based shape sensing, we propose a method that employs only two outer cores arranged non-collinearly with the central core in an MC-FBG array, together with precise geometric calibration of these two cores. Leveraging the underlying geometry, we derive analytical expressions for the curvature magnitude and bending angle specific to this two-outer-core configuration. The calibration compensates for manufacturing tolerances and packaging-induced deviations in core spacings and angles, thereby reducing systematic bias in the strain-to-curvature mapping. Building on these components, our reconstruction pipeline accurately recovers both 2D and 3D standard shapes and provides a uniform basis for comparing alternative outer-core layouts. Overall, the proposed architecture delivers high accuracy with lower hardware complexity and computational burden, making it well suited for real-time, high-precision, and resource-efficient endoscopic shape sensing.

2. Sensing Principle

2.1. Bending-Strain Decoupling

Under the combined effects of temperature and strain, the Bragg wavelength shift of an FBG can be expressed as

$$\Delta\lambda_B = \lambda_B[(\alpha + \xi) \cdot \Delta T + (1 - P_e) \cdot \varepsilon] \tag{1}$$

where α is the thermal expansion coefficient, ξ is the thermo-optic coefficient, ΔT denotes the temperature variation, P_e is the effective photo-elastic coefficient, ε is the strain, and λ_B is the Bragg wavelength.

For the central core of an MCF, the FBG is located on the neutral axis. Therefore, bending does not introduce additional strain at the central core, and the wavelength shift is mainly affected by temperature and uniform axial strain. For the central core (indexed by 1), the wavelength shift is written as

$$\Delta\lambda_{B,1} = \lambda_{B,1}[(\alpha + \xi) \cdot \Delta T + (1 - P_e) \cdot \varepsilon_a] \tag{2}$$

where ε_a denotes the uniform axial strain induced by stretching/compression.

For an outer core i, the strain measured by the FBG contains contributions from axial strain and bending-induced strain. In addition, torsion primarily generates shear strain in a circular fiber, and its contribution to the axial strain sensed by FBGs is negligible for parallel-aligned cores, thus the torsion-induced axial strain term can be ignored ($\varepsilon_\tau \approx 0$) [28]. Accordingly, the wavelength shifts in outer core i is expressed as

$$\Delta\lambda_{B,i} = \lambda_{B,i}[(\alpha + \xi) \cdot \Delta T + (1 - P_e) \cdot (\varepsilon_a + \varepsilon_{b,i} + \varepsilon_\tau)]. \tag{3}$$

where $\varepsilon_{b,i}$ denotes the bending strain in outer core i.

Since the FBGs at the same axial location are fabricated to have approximately identical Bragg wavelengths, we assume $\lambda_{B,1} = \lambda_{B,i} = \lambda_B$. Subtracting (2) from (3) removes the common-mode temperature and uniform axial-strain terms, yielding a differential expression for bending strain:

$$\Delta\lambda_{B,i} - \Delta\lambda_{B,1} = \lambda_B(1 - P_e) \cdot \varepsilon_{b,i}. \tag{4}$$

Therefore, the bending strain $\varepsilon_{b,i}$ can be accurately obtained from the differential wavelength shift together with a sensitivity calibration.

2.2. Two-Core Curvature Estimation

In MC-FBG-array-based shape sensing, the curvature κ and bending angle θ_B are first estimated from the discrete bending strains measured in the outer cores, after which the 3D centerline is reconstructed by a moving-frame method. According to Euler-Bernoulli beam theory [29], the bending strain in outer core i can be written as

$$\varepsilon_{b,i} = \kappa r_i \cos(\theta_B - \theta_i + \theta_{\tau_0}), i \in \{2, 3, 4, 5, 6, 7\} \tag{5}$$

where r_i is the core spacing, θ_i is the angular position of outer core i in the cross-section, and θ_{τ_0} represents a small initial angular offset (e.g., introduced during fabrication/packaging) that can be compensated through geometric calibration.

In conventional seven-core fiber, the outer cores are typically arranged in geometries such as regular hexagon, equilateral triangle (the most common), rectangle, or right triangle, as illustrated in Figure 1b. When the geometric parameters are assumed to take their theoretical values, the apparent curvature method [21] can be used to compute the curvature

and bending angle from the measured strains of multiple outer cores. However, since only κ and θ_B are unknowns in Equation (5), two independent equations are sufficient to determine them. As reported in [30], the accuracy of shape reconstruction is largely influenced by strain measurement errors; hence, using a greater number of outer cores introduces more sources of error. In addition, the internal geometric parameters of the MCF after packaging can be calibrated using our previously reported method [28] to reduce measurement errors in curvature and bending angle. Therefore, a shape sensing and reconstruction method based on two calibrated outer cores can effectively reduce computational complexity while improving measurement accuracy.

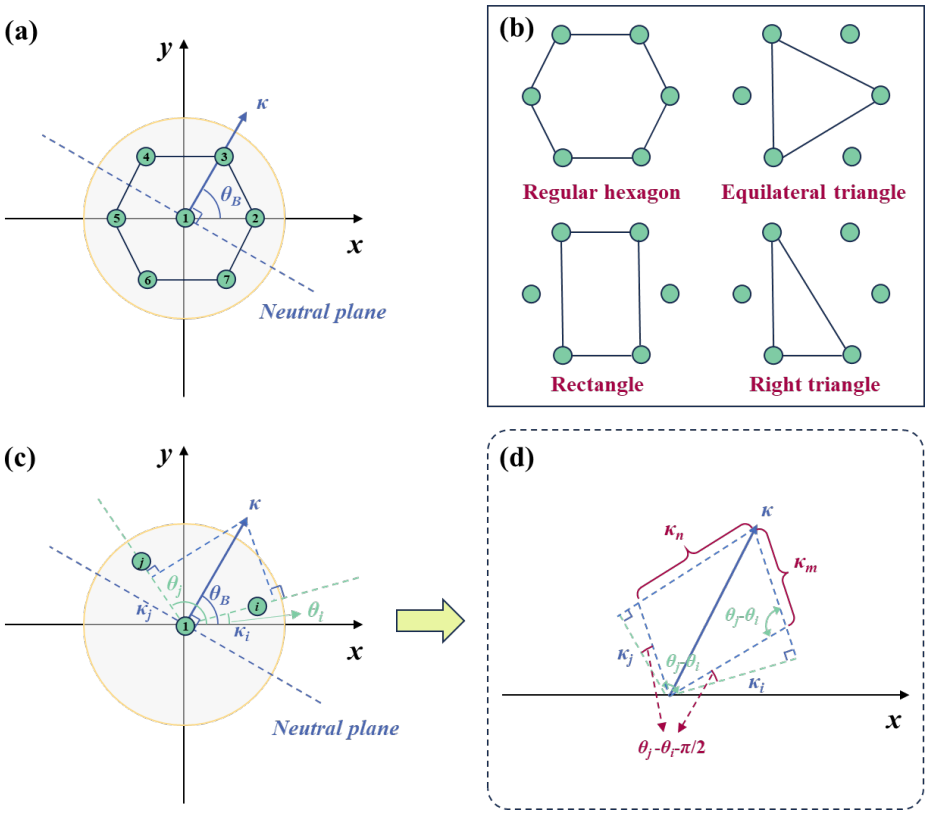


Figure 1. (**a**) Schematic of the cross-sectional configuration of a seven-core fiber. (**b**) Typical configurations of four commonly used outer-core arrangements. (**c**) Schematic diagram illustrating the principle of the two selected outer cores. (**d**) Geometric relationship diagram for curvature analysis.

Taking two outer cores i and j arranged non-collinearly with the central core in MCF as an example (as illustrated in Figure 1c), the projection of the curvature on the line connecting each outer core to the central core can be expressed as:

$$\kappa_{i/j} = \kappa\cos\left(\theta_B - \theta_{i/j} + \theta_{\tau_0}\right) = \frac{\varepsilon_{i/j} - \varepsilon_1}{r_{i/j}} \tag{6}$$

As shown in Figure 1d, a geometric relationship can be established in the right triangle:

$$\kappa_{m/n} = \frac{\kappa_{i/j}}{\cos\left(\theta_j - \theta_i - \pi/2\right)} = \frac{\kappa_{i/j}}{\sin\left(\theta_j - \theta_i\right)} \tag{7}$$

Accordingly, based on the cosine law, the curvature magnitude can be derived as:

$$\kappa = \sqrt{\kappa_m^2 + \kappa_n^2 - 2{\cdot}\kappa_m{\cdot}\kappa_n\cos\left(\theta_j - \theta_i\right)} \tag{8}$$

and the bending angle is given by:

$$\theta_B = \theta_i + \arccos\left(\frac{\kappa_i}{\kappa}\right) \tag{9}$$

Thus, the projections of the curvature in the local Cartesian coordinate system can be expressed as:

$$\kappa_1 = \kappa \cdot \cos\theta_B, \kappa_2 = \kappa \cdot \sin\theta_B \tag{10}$$

2.3. Three-Dimensional Shape Reconstruction

To enhance the effective spatial resolution, κ_1 and κ_2 are interpolated using cubic splines to yield $\kappa_1(s)$ and $\kappa_2(s)$, with s representing the arc location of the curve. Subsequently, the Bishop frame [21] is adopted as the moving frame for reconstruction, in which the unit tangent vector $\boldsymbol{T}$ and two mutually orthogonal normal vectors $\boldsymbol{N_1}$ and $\boldsymbol{N_2}$ satisfy the following relationship:

$$\begin{bmatrix} \boldsymbol{T}' \\ \boldsymbol{N}_1' \\ \boldsymbol{N}_2' \end{bmatrix} = \begin{bmatrix} 0 & \kappa_1(s) & \kappa_2(s) \\ -\kappa_1(s) & 0 & 0 \\ -\kappa_2(s) & 0 & 0 \end{bmatrix} \begin{bmatrix} \boldsymbol{T} \\ \boldsymbol{N}_1 \\ \boldsymbol{N}_2 \end{bmatrix} \tag{11}$$

By integrating the iteratively computed unit tangent vectors, the 3D spatial coordinates along the shape sensor can be reconstructed as:

$$\mathbf{p}(s) = \mathbf{p}(0) + \int_0^s \boldsymbol{T}(u)du \tag{12}$$

2.4. Error Evaluation

To quantitatively evaluate the reconstruction performance, we compare the reconstructed centerline with the ground truth centerline sampled at the same arc locations. Let $\mathbf{p}_i \in \mathrm{R}^3$ and $\mathbf{p}_i^{gt} \in \mathrm{R}^3$ denote the reconstructed and ground truth coordinates at the i-th sample point $(i = 1, \ldots, N)$, respectively, where N is the total number of sample points after interpolation. The absolute position error is defined as

$$e_i = \left\| \mathbf{p}_i - \mathbf{p}_i^{gt} \right\|_2. \tag{13}$$

Based on $\{e_i\}$, the maximum absolute error and absolute RMSE are computed as

$$e_{max} = \max_{1 \le i \le N} e_i, RMSE_{abs} = \sqrt{\frac{1}{N}\sum_{i=1}^{N} e_i^2}. \tag{14}$$

To enable fair comparison across shapes of different total sensing length, we further define the relative error by dividing e_i by the arc location s of the evaluated centerline:

$$r_i = \frac{e_i}{s}. \tag{15}$$

Accordingly, the maximum relative error and relative RMSE are given by

$$r_{\max} = \max_{1 \le i \le N} r_i, \mathrm{RMSE}_{rel} = \sqrt{\frac{1}{N}\sum_{i=1}^{N} r_i^2} = \frac{\mathrm{RMSE}_{abs}}{s}. \tag{16}$$

3. Experiments and Results

3.1. Experimental Setup

Building on the sensing principle in Section 2, we implement the proposed two-outer-core reconstruction framework in a complete endoscopic shape-sensing platform, which enables wavelength demodulation and 3D centerline reconstruction within a unified experimental chain.

As shown in Figure 2a, the MC-FBG array based 3D shape sensing system consists of an endoscope (CONCEMED Co., Ltd., Shenzhen, China) integrated with a 3D shape sensor, a fan-in/fan-out (FIFO) device for the MCF (OPTOWEAVE Co., Ltd., Shanghai, China), a seven-core MCF (YOFC Co., Ltd., Wuhan, China) with a nominal core spacing of 41.5 μm and a regular hexagonal outer-core layout, an eight-channel FBG interrogator (Wuhan Smart Fiber Co., Ltd., Wuhan, China) with a wavelength range of 1522–1572 nm, a sampling rate of 100 Hz, and a wavelength resolution of 1 pm, as well as a host PC. The cross-sectional configuration of the seven-core fiber is shown in the inset at the upper right of Figure 2a. In this work, core 1 (central core) and two outer cores, core 2 and core 4, are selected as the sensing cores.

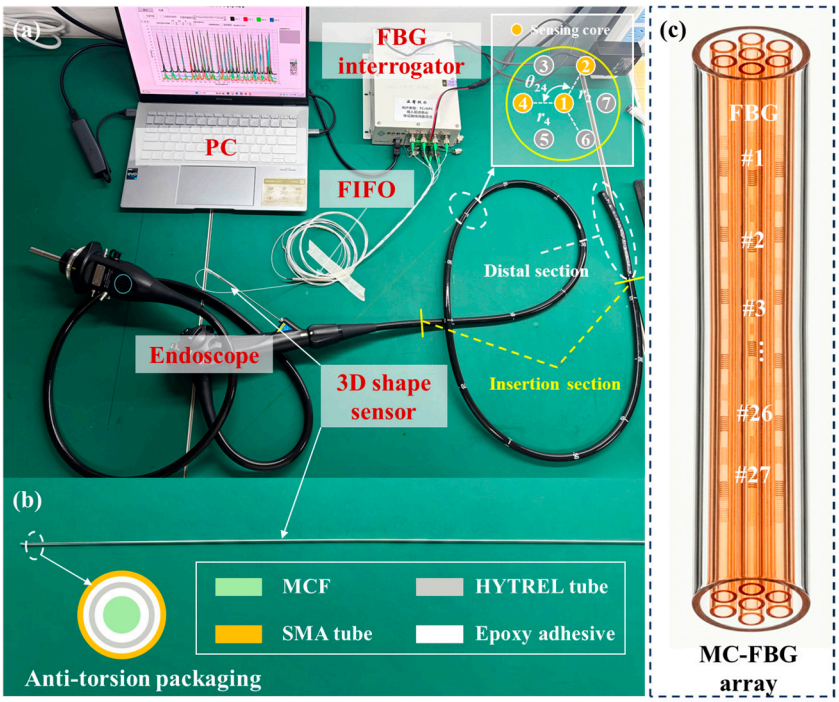


Figure 2. (**a**) Experimental setup for endoscope shape sensing. (**b**) Anti-torsion packaging of the 3D shape sensor. (**c**) Schematic diagram of the MC-FBG array structure.

The 3D shape sensor was fabricated by packaging the MC-FBG array following our previous work [28]. As shown in Figure 2c, the FBGs were fabricated using a phase-mask technique, and at each axial location, FBGs with the same grating period were written in all cores of the MCF to ensure consistent Bragg wavelengths across cores. As illustrated in Figure 2b, an anti-torsion packaging structure was adopted to minimize the influence of external torsion on the initial angular offset term in Equation (5). Specifically, the MCF was fixed at the center of a HYTREL tube with an inner diameter of 0.4 mm and an outer diameter of 0.9 mm using an epoxy adhesive (EPO-TEK MED-301, Epoxy Tech., Inc., Billerica, MA, USA), which ensures that the central core remains close to the neutral axis of the overall structure. The HYTREL tube was then inserted into an SMA tube made of nickel–titanium alloy with an outer diameter of 1.2 mm and an inner diameter of 1.0 mm,

which improves resistance to external torsion and axial stretching. The characterization results of the fabricated MC-FBG array are provided in Section 3.2. The FIFO connects the shape sensor to the interrogator for Bragg-wavelength demodulation, while the PC executes the 3D shape-reconstruction algorithm.

3.2. Testing and Calibration

With the endoscopic sensing platform established, accurate estimation of curvature and bending angle, as well as subsequent shape reconstruction, requires knowledge of the sensing-point locations along the fiber and the cross-sectional geometry of the selected cores. Therefore, before performing curvature interpolation, we experimentally characterized the MC-FBG array and calibrated the geometric parameters of the two selected outer cores, including the core spacing and core angles.

The reflection spectrum of core 1 measured by the FBG interrogator is shown in Figure 3a. Each core in the MC-FBG array contains 27 FBGs. The Bragg-wavelength spacing between the first five FBGs is approximately 3 nm, for example, 3.23 nm between sensors #1 and #2. This spectral allocation corresponds to the distal section of the endoscope, where larger bending deformation is expected. A wider wavelength spacing is therefore assigned to reduce the risk of spectral overlap and crosstalk between adjacent FBG signals under large curvature. In contrast, the wavelength spacing for the remaining FBGs is approximately 1.5 nm, for example, 1.41 nm between sensors #5 and #6. These sensors correspond to the insertion section of the endoscope, which generally experiences smaller bending deformation. Consequently, a narrower wavelength allocation is sufficient in this region.

Meanwhile, the axial spatial distribution of core 1 was characterized using an OFDR system, as shown in Figure 3b. Each FBG was designed with a length of 5 mm to mitigate the influence of non-uniform strain during sensing [31]. The total sensing length of the array is 1235.91 mm. The spacing between adjacent FBGs is approximately 25 mm for the first five sensors, for example, 24.99 mm between sensors #3 and #4. This denser layout is used in the distal section, which has a length of 110 mm and undergoes larger bending, so a higher sensing-point density is required. For the remaining sensors, the spacing is approximately 50 mm, for example, 49.61 mm between sensors #15 and #16. This reduced density is adopted in the insertion section where bending is comparatively smaller.

The combined wavelength and spatial layout help avoid spectral overlap between neighboring FBGs in the highly deformable distal section of the endoscope. A larger spacing of approximately 100 mm is observed between sensors #7 and #8 in Figure 3b due to a missing FBG during fabrication. Nevertheless, as demonstrated by the shape sensing and reconstruction results in Section 3.3, this irregularity has negligible impact on the overall performance.

According to Equation (5), the geometric parameters of the two selected outer cores, including the core spacing and their relative core angle, can be calibrated by exploiting the cosine dependence of the Bragg wavelength shift on the bending angle. Figure 3c presents the raw data and the corresponding cosine fits for cores 2 and 4 at sensing point #1. The fitted results yield $r_2 = 40.48\,\mu m$, $r_4 = 39.74\,\mu m$, and $\theta_{24} = \theta_4 - \theta_2 = 130.29^\circ$. Similarly, as shown in Figure 3d, the calibrated parameters at sensing point #27 are $r_2 = 41.09\,\mu m$, $r_4 = 41.34\,\mu m$, and $\theta_{24} = 126.39^\circ$.

Furthermore, we performed calibration for cores 2 and 4 at all sensing points along the MCF. The resulting distributions of the core spacing and the relative core angle are shown in Figures 3e and 3f, respectively. The calibrated core spacings of cores 2 and 4 deviate from the nominal value of 41.5 μm, and the maximum deviation is within ±10 μm. Notably, the core spacing variations in the two outer cores exhibit highly consistent trends,

suggesting that the core spacing deviation is mainly due to fabrication tolerances of the MCF. The calibrated relative core angle θ_{24} remains close to the nominal value of 120°. Larger deviations are observed at sensing points #1 and #2, which is likely caused by systematic errors introduced by the calibration fixture near the fiber end.

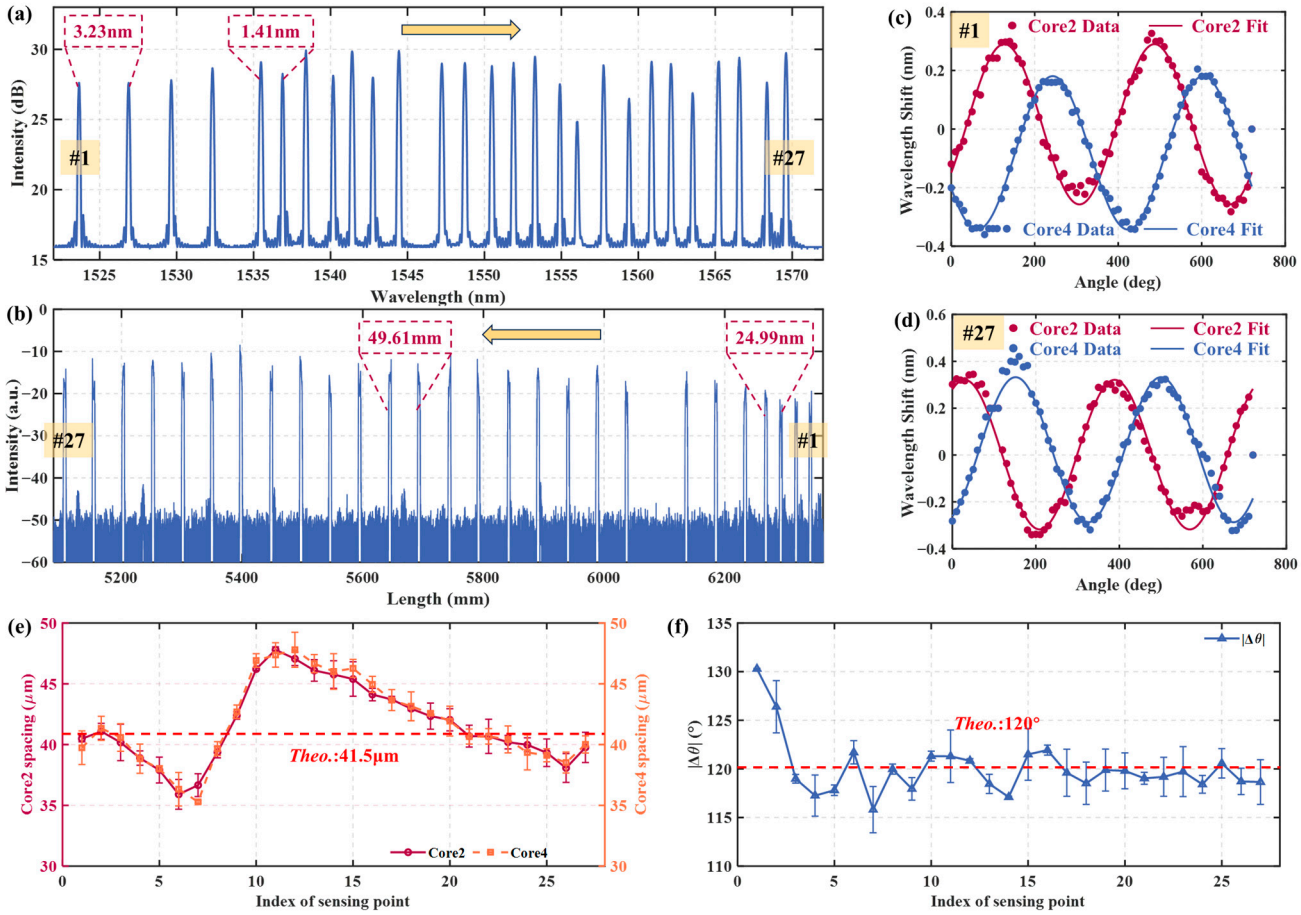


Figure 3. (**a**) Reflection spectrum of core 1 in the MC-FBG array. (**b**) Spatial distribution of core 1 within the MC-FBG array. (**c**) Geometric parameter measurement results at the 1st sensing point. (**d**) Geometric parameter measurement results at the 27th sensing point. (**e**) Distribution of the core spacing for core 2 and core 4 at all sensing points after calibration. (**f**) Distribution of the relative core angle at each sensing point between Core 2 and Core 4 after calibration.

Overall, these results indicate that the outer-core geometric parameters of the MCF deviate slightly from their nominal specifications. Therefore, geometric calibration is necessary to obtain accurate estimates of curvature and bending angle for reliable 3D shape reconstruction.

3.3. Standard Shape Sensing

After obtaining the calibrated geometric parameters and sensing-point locations, we proceed to validate the proposed two-outer-core strategy by benchmarking its reconstruction accuracy on canonical shapes. To this end, both 2D and 3D standard shapes were reconstructed using three different outer-core configurations, namely an equilateral triangle, a regular hexagon, and the proposed two-core configuration with a 120° core separation. For the 2D case, a circular arc with a radius of 300 mm was adopted. As shown in Figure 4(a1,a2), without geometric calibration the deviations of the estimated curvature and bending angle from the theoretical values (3.3×10^{-3} mm^{-1} and 0 rad) are comparable across the three configurations considered, confirming that the proposed non-collinear

two-outer-core scheme already yields valid estimates. After calibration, the deviations observed in the two-outer-core case are significantly reduced, indicating that the calibration procedure effectively improves reconstruction accuracy. This improvement is also evident in the reconstruction results: as shown in Figure 4(a3), the calibrated two-outer-core scheme produces a 2D curve visibly closer to the ground truth than the other three configurations; the quantitative error analysis in Figure 4(a4) and Table 1 indicates a maximum relative error of only 1.62%. A similar conclusion holds for a 3D shape-specifically, a left-handed cylindrical helix with a base radius of 100 mm and a pitch of 50 mm (see in Figure 4(b1–b4)); the maximum relative error is only 2.81%. These results show that shape sensing using two calibrated outer cores in an MC-FBG array effectively improves reconstruction accuracy while maintaining low hardware complexity.

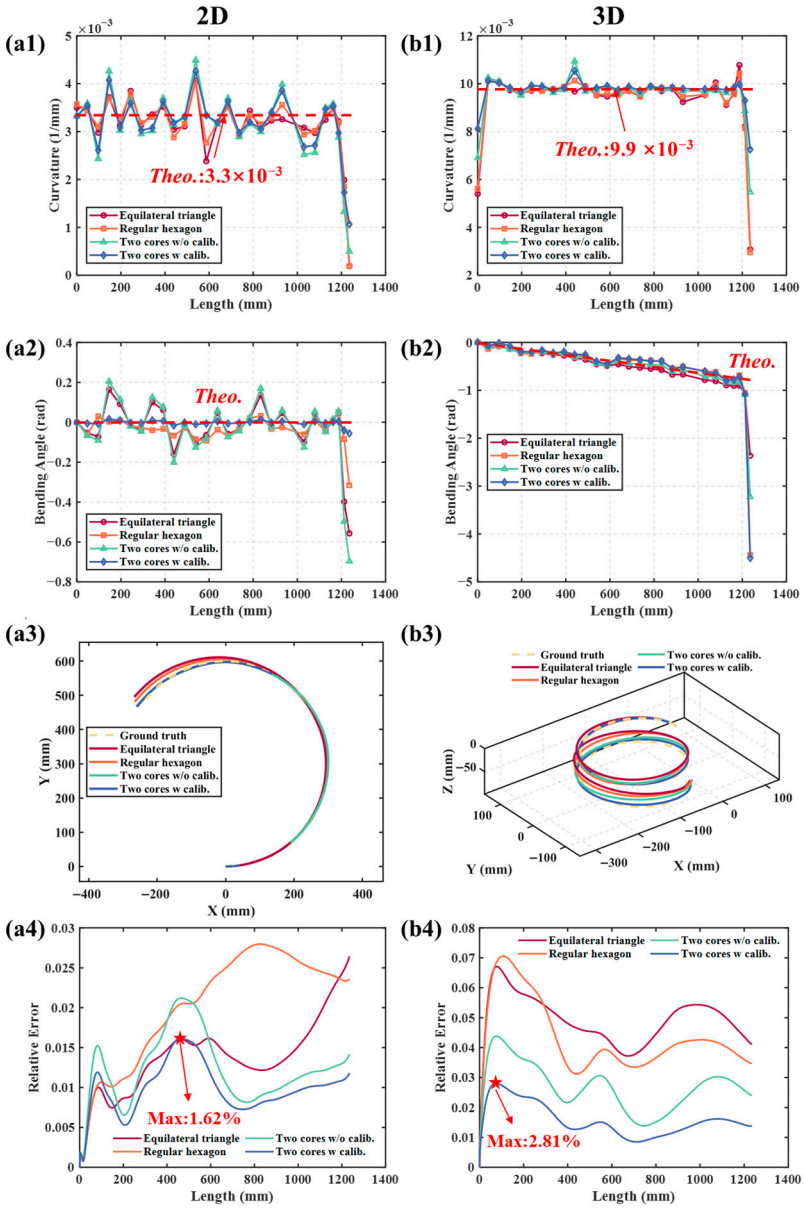


Figure 4. (**a1**–**a4**) show the curvature, bending angle, shape reconstruction, and error analysis results obtained using different outer-core configurations for the 2D circular-arc measurement. (**b1**–**b4**) show the corresponding results for the 3D helical measurement.

Table 1. Shape-reconstruction error under the four configurations.

Dimension	Configuration	Max. Absolute Error (mm)	RMSE Absolute Error (mm)	Max. Relative Error (%)	RMSE Relative Error (%)
2D	Equilateral triangle	32.66	12.49	2.64	1.46
	Regular hexagon	29.15	17.76	2.80	2.15
	Two cores w/o calib.	17.52	8.75	2.12	1.30
	Two cores w calib.	**14.60**	**7.24**	**1.62**	**1.04**
3D	Equilateral triangle	50.78	34.38	6.71	5.00
	Regular hexagon	40.03	28.04	7.06	4.50
	Two cores w/o calib.	29.78	17.99	4.38	2.79
	Two cores w calib.	**17.16**	**9.94**	**2.81**	**1.67**

3.4. Arbitrary Shape Sensing

While the canonical-shape tests establish baseline accuracy, practical endoscopic use further requires the sensor to remain reliable after being integrated into the endoscope and operated under realistic manipulation. In clinical procedures, the distal tip is typically the only part directly visualized, whereas the shaft configuration inside the body is largely invisible. This makes shaft looping difficult to anticipate and motivates evaluating reconstruction performance on representative loop patterns that commonly occur during insertion and steering.

To demonstrate the applicability of the proposed method to realistic endoscopic shape sensing, we reconstructed three frequently observed loop types formed within the body, including the α-loop, the reversed α-loop, and the N-loop. The reconstructed shapes closely matched the corresponding endoscopic images, as shown in Figure 5(a1–c2). We further tested the method on arbitrary 3D configurations and obtained similarly high-fidelity reconstructions, as shown in Figure 5(d1,d2). Collectively, these results indicate that the proposed method can accurately capture endoscope configurations under realistic operating conditions.

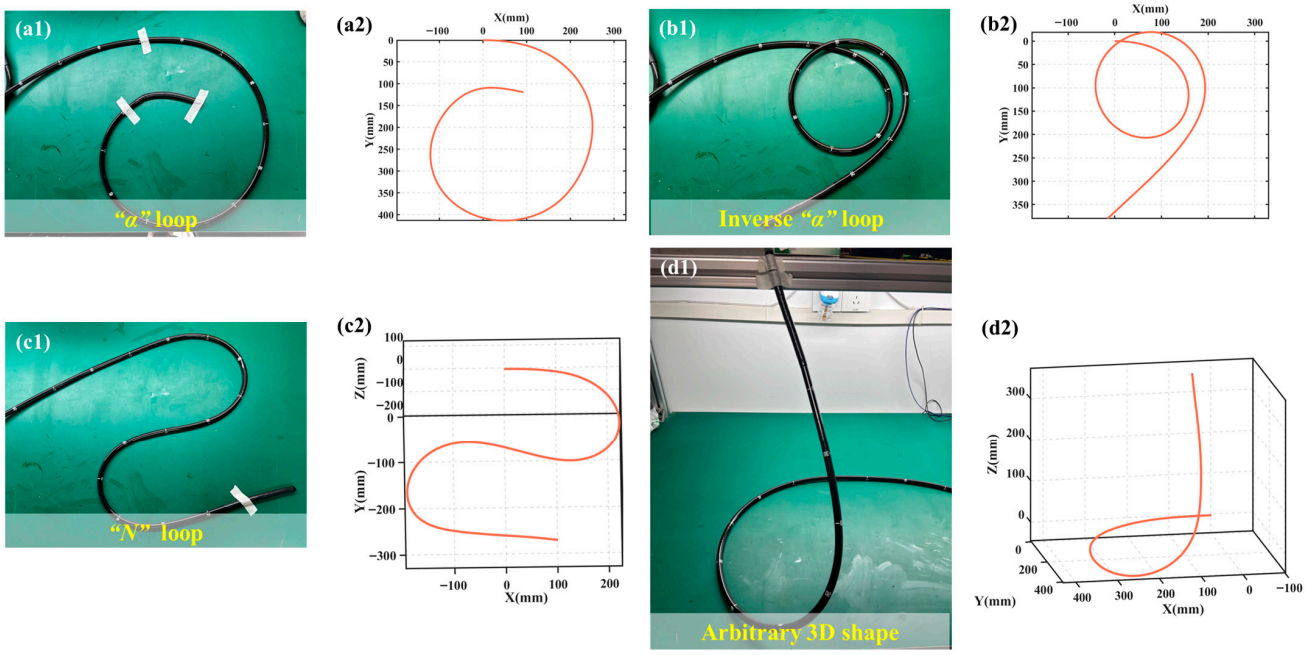


Figure 5. (**a1**–**d1**) Real images of endoscope shapes. (**a2**–**d2**) Corresponding reconstructed shapes using two outer cores for the "α" loop, reversed "α" loop, "N" loop, and an arbitrary 3D shape.

It is worth noting that, for these endoscope-relevant configurations, an accurate 3D ground truth of the shaft centerline inside the body is not directly available in our current experimental setting. Therefore, in addition to the overall visual agreement, we further assess the reconstruction quality using qualitative consistency criteria that can be verified from the images in Figure 5. In particular, the reconstructed loops reproduce the expected self-intersection topology and the relative locations of crossing points observed in the corresponding endoscopic images. For the α-loop and reversed α-loop in Figure 5(a1–b2), the reconstructed centerlines correctly capture the single crossover and its position along the loop. For the N-loop in Figure 5(c1,c2), the reconstruction preserves the characteristic crossing structure and the relative ordering of segments around the intersection. For the arbitrary 3D configuration in Figure 5(d1,d2), the reconstructed centerline remains geometrically plausible and consistent with the observed global shape, including the location where the shaft passes over itself. These qualitative agreements support the applicability of the proposed method in realistic endoscopic scenarios where direct ground truth measurement is challenging.

3.5. Anti-Environmental Interference Capability

To evaluate the shape-reconstruction performance of the proposed method under environmental disturbances, we conducted robustness tests on the 3D shape sensor. Since the anti-torsion packaging described in Section 3.1 effectively suppresses the influence of external torsion and axial stretching, this sub-section focuses on the effect of temperature variations on reconstruction results.

Considering that the typical operating temperature of endoscopic procedures is 30–42 °C, we performed experiments over a wider range of 25–81 °C to fully cover and exceed the clinical range. The 3D shape sensor was embedded and fixed in the groove of a standard-shape fixture, namely a left-handed cylindrical helix with a base radius of 100 mm and a pitch of 50 mm. The fixture was placed inside a temperature chamber, and the Bragg wavelengths of cores 1, 2, and 4 were recorded every 4 °C.

The measured wavelength shifts as a function of temperature are shown in Figure 6a. The temperature sensitivities of cores 1, 2, and 4 are highly consistent and are approximately 10 pm/°C, which supports the feasibility of the temperature compensation strategy described in Section 2.1 using the central core as a reference. The reconstructed shapes at different temperatures are compared in Figure 6b. The reconstructed centerlines nearly overlap across the entire temperature range, with only minor discrepancies observed near the distal end, as highlighted in Figure 6c.

We further quantified the influence of temperature on reconstruction accuracy, as summarized in Figure 6d. Across all tested temperatures, the variation in the maximum absolute reconstruction error remains within $\pm$1.5 mm, and the variation in the absolute RMSE remains within $\pm$1.0 mm. For the relative metrics, the variation in the maximum relative error is within $\pm$0.15%, and the variation in the relative RMSE is within $\pm$0.12%. These results demonstrate that the proposed method maintains stable reconstruction accuracy under temperature variations, indicating good robustness for practical use.

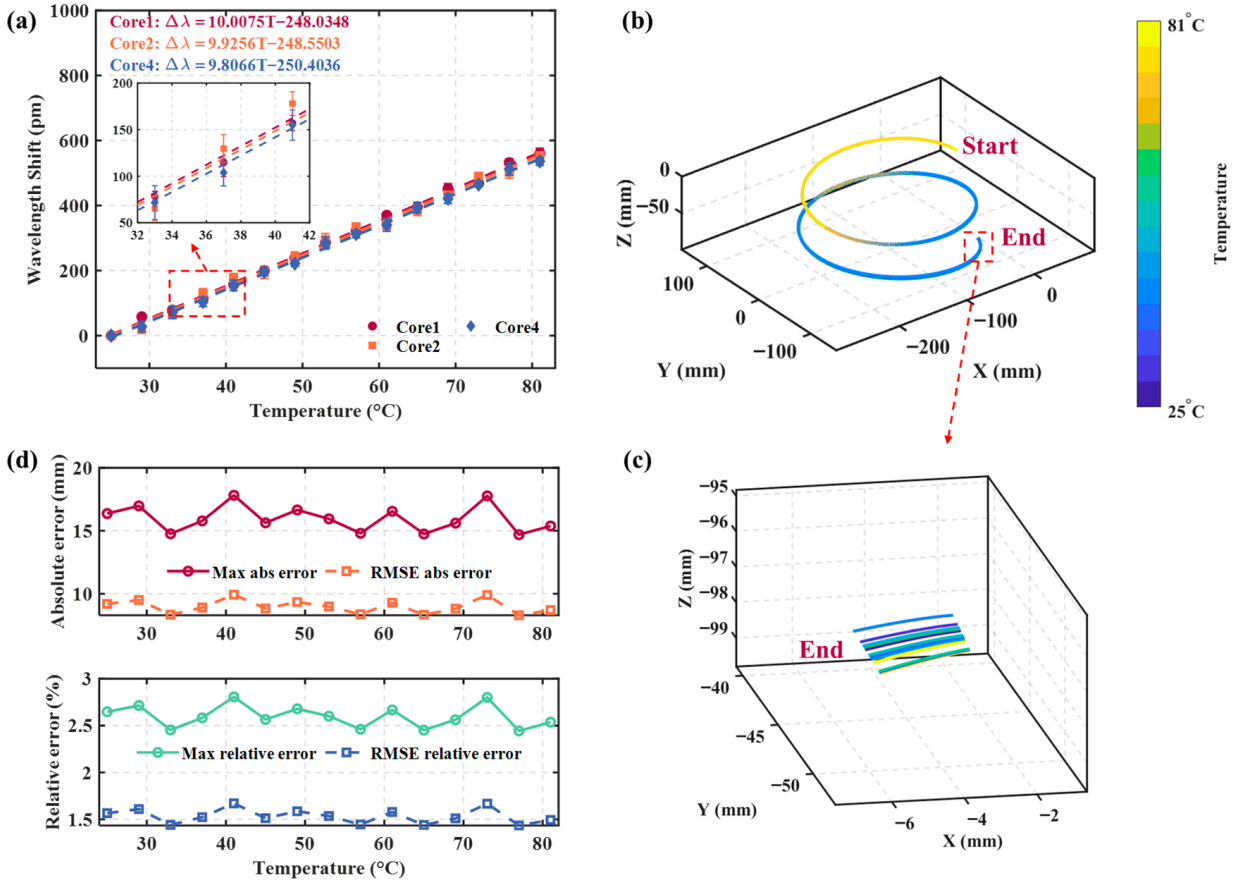


Figure 6. (**a**) The Bragg-wavelength shifts in the FBGs in cores 1, 2, and 4 over a temperature range of 25–81 °C. (**b**) Reconstructed shapes of a left-handed cylindrical helix with a base radius of 100 mm and a pitch of 50 mm at different temperatures. (**c**) Enlarged view of the distal-end region of the reconstruction results in (**b**). (**d**) Influence of temperature on the absolute and relative reconstruction errors.

4. Conclusions

In this work, we present a lightweight approach to endoscopic 3D shape sensing that uses only two non-collinear outer cores, geometrically referenced to the central core of an MC-FBG array. By exploiting inter-core geometric constraints, we derive closed-form expressions for curvature and bending angle and introduce geometric-parameter calibration to suppress systematic bias and error propagation. On canonical shapes, the method achieves maximum relative position errors of 1.62% for a 2D circular arc and 2.81% for a 3D helix, and we additionally report RMSE-based metrics for a more complete quantitative evaluation. For endoscope-relevant configurations including the α-loop, reversed α-loop, and N-loop, the reconstructions preserve the expected loop topology and crossing-point locations observed in endoscopic images. Moreover, temperature tests over 25–81 °C show stable reconstruction accuracy after compensation using the central core as a reference. Together, these results demonstrate a low-resource and high-fidelity solution that is well suited for practical endoscopic shape sensing.

Author Contributions: Conceptualization, C.T. and B.X.; methodology, C.T. and B.X.; software, C.T., X.X. and J.Z.; validation, C.T., B.X. and W.Z.; formal analysis, C.T. and B.X.; investigation, C.T. and B.X.; resources, W.Z.; data curation, B.X. and C.T.; writing—original draft preparation, C.T. and B.X.; writing—review and editing, Z.Y., Y.H. and W.Z.; visualization, C.T. and B.X.; supervision, Z.Y. and Y.H.; project administration, Z.Y.; funding acquisition, Z.Y. All authors have read and agreed to the published version of the manuscript.

Funding: This work was supported by the Concept Validation Project of the Hubei Optics Valley Laboratory under Grant OVL2025YZ006.

Data Availability Statement: The original contributions presented in this study are included in the article. Further inquiries can be directed to the corresponding authors.

Conflicts of Interest: The authors declare that the research was conducted in the absence of any commercial or financial relationships that could be construed as a potential conflict of interest.

References

1. Fu, Z.; Jin, Z.; Zhang, C.; He, Z.; Zha, Z.; Hu, C.; Gan, T.; Yan, Q.; Wang, P.; Ye, X. The future of endoscopic navigation: A review of advanced endoscopic vision technology. *IEEE Access* **2021**, *9*, 41144–41167. [CrossRef]
2. Wei, R.; Li, B.; Zhong, F.; Mo, H.; Dou, Q.; Liu, Y.-H.; Sun, D. Absolute monocular depth estimation on robotic visual and kinematics data via self-supervised learning. *IEEE Trans. Autom. Sci. Eng.* **2025**, *22*, 4269–4282. [CrossRef]
3. Chen, Z.; Renda, F.; Le Gall, A.; Mocellin, L.; Bernabei, M.; Dangel, T.; Ciuti, G.; Cianchetti, M.; Stefanini, C. Data-driven methods applied to soft robot modeling and control: A review. *IEEE Trans. Autom. Sci. Eng.* **2025**, *22*, 2241–2256. [CrossRef]
4. Jang, M.; Jeon, H.J.; Kim, B.K.; Moon, H.; Keum, B.; Kim, J. Real-time three-dimensional endoscope shape monitoring using long and twist-suppressed fiber Bragg grating sensors. *IEEE/ASME Trans. Mechatron.* **2025**, *30*, 6467–6477. [CrossRef]
5. Spier, B.J.; Benson, M.; Pfau, P.R.; Nelligan, G.; Lucey, M.R.; Gaumnitz, E.A. Colonoscopy training in gastroenterology fellowships: Determining competence. *Gastrointest. Endosc.* **2010**, *71*, 319–324. [CrossRef]
6. Gangwani, M.K.; Haghbin, H.; Ishtiaq, R.; Hasan, F.; Dillard, J.; Jaber, F.; Dahiya, D.S.; Ali, H.; Salim, S.; Lee-Smith, W.; et al. Single versus second observer vs artificial intelligence to increase the adenoma detection rate of colonoscopy: A network analysis. *Dig. Dis. Sci.* **2024**, *69*, 1380–1388. [CrossRef]
7. Lu, Y.; Wei, R.; Li, B.; Chen, W.; Zhou, J.; Dou, Q.; Sun, D.; Liu, Y.-H. Autonomous intelligent navigation for flexible endoscopy using monocular depth guidance and 3-D shape planning. In Proceedings of the IEEE International Conference on Robotics and Automation (ICRA), London, UK, 29 May–2 June 2023; pp. 1–7.
8. Martin, J.W.; Scaglioni, B.; Norton, J.C.; Subramanian, V.; Arezzo, A.; Obstein, K.L.; Valdastri, P. Enabling the future of colonoscopy with intelligent and autonomous magnetic manipulation. *Nat. Mach. Intell.* **2020**, *2*, 595–606. [CrossRef]
9. Huang, H.-E.; Yen, S.-Y.; Chu, C.-F.; Suk, F.-M.; Lien, G.-S.; Liu, C.-W. Autonomous navigation of a magnetic colonoscope using force sensing and a heuristic search algorithm. *Sci. Rep.* **2021**, *11*, 16491. [CrossRef]
10. Centurelli, A.; Arleo, L.; Rizzo, A.; Tolu, S.; Laschi, C.; Falotico, E. Closed-Loop Dynamic Control of a Soft Manipulator Using Deep Reinforcement Learning. *IEEE Robot. Autom. Lett.* **2022**, *7*, 4741–4748. [CrossRef]
11. Dürrbeck, C.; Schuster, S.; Sauer, B.C.; Abu-Hossin, N.; Strnad, V.; Fietkau, R.; Bert, C. Localization of reference points in electromagnetic tracking data and their application for treatment error detection in interstitial breast brachytherapy. *Med. Phys.* **2023**, *50*, 5772–5783. [CrossRef]
12. Li, W.; Ma, Q.; Liu, C.; Zhang, Y.; Wu, X.; Wang, J.; Gao, S.; Qiu, T.; Liu, T.; Xiao, Q.; et al. Intelligent metasurface system for automatic tracking of moving targets and wireless communications based on computer vision. *Nat. Commun.* **2023**, *14*, 989. [CrossRef] [PubMed]
13. Mehta, A.C.; Hood, K.L.; Schwarz, Y.; Solomon, S.B. The evolutional history of electromagnetic navigation bronchoscopy: State of the art. *Chest* **2018**, *154*, 935–947. [CrossRef] [PubMed]
14. Keetha, N.; Karhade, J.; Jatavallabhula, K.M.; Yang, G.; Scherer, S.; Ramanan, D.; Luiten, J. SplaTAM: Splat track & map 3D Gaussians for dense RGB-D SLAM. In Proceedings of the IEEE/CVF Conference on Computer Vision and Pattern Recognition (CVPR), Seattle, WA, USA, 16–22 June 2024; pp. 21357–21366.
15. Yasunaga, A.; Saito, H.; Mori, S. User-in-the-loop view sampling with error peaking visualization. In Proceedings of the IEEE International Conference on Image Processing (ICIP), Anchorage, AK, USA, 14–17 September 2025; pp. 1151–1156.
16. Ma, X.; Wu, X.; Zhang, L.; Shen, S. Enhancing SplaTAM performance through dynamic learning rate decay and optimized keyframe selection. In Proceedings of the IEEE International Conference on Robotics and Biomimetics (ROBIO), Bangkok, Thailand, 10–14 December 2024; pp. 1972–1977.
17. Zhao, W.; Xiao, X.; Zuo, J.; Sun, Z.; Liu, H.; Zhang, Y.; Zhang, M.; Yan, Z.; Sun, Q. DFBG-based shape sensor for large-curvature reconstruction. In *29th International Conference on Optical Fiber Sensors*; SPIE: Bellingham, WA, USA, 2025; Volume 13639, p. 136398D.
18. Jiang, Q.; Li, J.; Masood, D. Fiber-optic-based force and shape sensing in surgical robots: A review. *Sens. Rev.* **2023**, *43*, 52–71. [CrossRef]
19. Meng, Y.; Sui, R.; Liang, W.; Zhong, H.; Shan, R.; Xiao, S.; Kong, Y.; Fu, C.; Wang, Y. Multicore fiber shape sensing based on optical frequency domain reflectometry parallel measurements. *J. Lightwave Technol.* **2024**, *42*, 3909–3917. [CrossRef]

20. Lamb, E.S.; Shi, Z.; Kremp, T.; DiGiovanni, D.J.; Westbrook, P.S. Shape sensing endoscope fiber. *Optica* **2024**, *11*, 1462–1467. [CrossRef]
21. Moore, J.P.; Rogge, M.D. Shape sensing using multi-core fiber optic cable and parametric curve solutions. *Opt. Express* **2012**, *20*, 2967–2973. [CrossRef]
22. Meng, Y.; Fu, C.; Du, C.; Chen, L.; Zhong, H.; Li, P.; Xu, B.; Du, B.; He, J.; Wang, Y. Shape sensing using two outer cores of multicore fiber and optical frequency domain reflectometer. *J. Lightwave Technol.* **2021**, *39*, 6624–6630. [CrossRef]
23. Lv, Y.; Li, H.; Yang, Z.; Yan, Z.; Zang, J.; Sun, Q. Highly accurate 3D shape sensing based on special fiber OFDR system assisted with ICP algorithm. In Proceedings of the 27th International Conference on Optical Fiber Sensors (OFS-27); Optica Publishing Group: Washington, DC, USA, 2022. Paper Tu1.7.
24. Li, S.; Li, Q.; Ding, Z.; Liu, K.; Wang, H.; Hua, P.; Guo, H.; Zhang, T.; Liu, J.; Jiang, J.; et al. Twist compensated, high accuracy and dynamic fiber optic shape sensing based on phase demodulation in optical frequency domain reflectometry. *Mech. Syst. Signal Process.* **2024**, *216*, 111462. [CrossRef]
25. Nguyen, N.; Parker, M.; Kara, O.C.; Alambeigi, F. Toward distributed fiber optic shape sensing of continuum manipulators: A cost-effective and simple manufacturing of sensor assembly. In Proceedings of the IEEE Sensors, Dallas, TX, USA, 30 October–2 November 2022; pp. 1–4.
26. Tavangarifard, M.; Ovalle, W.R.; Alambeigi, F. Single-fiber optical frequency domain reflectometry (OFDR) shape sensing of continuum manipulators with planar bending. In Proceedings of the IEEE International Conference on Robotics and Automation (ICRA), Atlanta, GA, USA, 19–23 May 2025; pp. 838–843.
27. Fu, C.; Xiao, S.; Meng, Y.; Shan, R.; Liang, W.; Zhong, H.; Liao, C.; Yin, X.; Wang, Y. OFDR shape sensor based on a femtosecond-laser-inscribed weak fiber Bragg grating array in a multicore fiber. *Opt. Lett.* **2024**, *49*, 1273–1276. [CrossRef]
28. Zhao, W.; Xiao, X.; Wu, J.; Sun, Z.; Liu, H.; Zhang, Y.; Wang, P.; Sun, Q.; Yan, Z. Twist-compensation and self-calibration method for high accuracy DFBG-based shape sensing. In Proceedings of the Optical Fiber Communications Conference and Exhibition (OFC), San Francisco, CA, USA, 30 March–3 April 2025; pp. 1–3.
29. Bauchau, O.A.; Craig, J.I. Euler–Bernoulli beam theory. In *Structural Analysis*; Bauchau, O.A., Craig, J.I., Eds.; Solid Mechanics and Its Applications; Springer: Dordrecht, The Netherlands, 2009; Volume 163.
30. Li, S.; Hua, P.; Ding, Z.; Liu, K.; Yang, Y.; Zhao, J.; Pan, M.; Guo, H.; Zhang, T.; Liu, L.; et al. Reconstruction error model of distributed shape sensing based on the reentered frame in OFDR. *Opt. Express* **2022**, *30*, 43255–43270. [CrossRef]
31. Rajabzadeh, A.; Heusdens, R.; Hendriks, R.C.; Groves, R.M. Calculation of the mean strain of smooth non-uniform strain fields using conventional FBG sensors. *J. Lightwave Technol.* **2018**, *36*, 3716–3725. [CrossRef]

Disclaimer/Publisher's Note: The statements, opinions and data contained in all publications are solely those of the individual author(s) and contributor(s) and not of MDPI and/or the editor(s). MDPI and/or the editor(s) disclaim responsibility for any injury to people or property resulting from any ideas, methods, instructions or products referred to in the content.